

Optimal linear inverse solution with multiple priors in diffuse optical tomography

Ang Li, Greg Boverman, Yiheng Zhang, Dana Brooks, Eric L. Miller, Misha E. Kilmer, Quan Zhang, Elizabeth M. C. Hillman, and David A. Boas

A general framework for incorporating single and multiple priors in diffuse optical tomography is described. We explore the use of this framework for simultaneously utilizing spatial and spectral priors in the context of imaging breast cancer. The utilization of magnetic resonance images of water and lipid content as a statistical spatial prior for the diffuse optical image reconstructions is also discussed. Simulations are performed to demonstrate the significant improvement in image quality afforded by combining spatial and spectral priors. © 2005 Optical Society of America

OCIS codes: 170.3010, 170.3880, 170.5280, 170.6510, 170.6960.

1. Introduction

Diffuse optical tomography (DOT) is a rapidly growing, new biomedical imaging method based on the propagation of near-infrared light through tissue.^{1–3} Owing to its sensitivity to hemoglobin, water, and lipid contrast in tissue, the technique has been widely used in the study of functional brain imaging,^{4–7} breast imaging,^{8–11} muscle,¹² and imaging of joint inflammation.^{13,14} The highly scattering nature of near-infrared photons through tissue leads to a complex forward and inverse problem. Furthermore, as the inverse imaging problem is ill posed and generally underdetermined, the image quality is compromised by poor spatial resolution and by sensitivity to measurement noise.

One approach to improve image quality is to incorporate prior information into the inverse problem. Arising from the portability of the instrument and the use of fiber optics, DOT can easily be combined and coregistered with other image modalities [for in-

stance, magnetic resonance image (MRI), ultrasound, and x ray]^{15–19} that can provide structural priors for the DOT image reconstruction. Another feature of tissue is that the optical properties vary as a function of source wavelength. The spectral content of the optical images enables the derivation of images of tissue physiology from the known spectra of tissue chromophores. These spectra can be exploited as a spectral prior in the image reconstruction, leading to a new imaging algorithm that can be used to reconstruct the chromophore image directly from the optical measurements at different wavelengths, rather than first reconstructing the optical properties and then deriving the chromophore images.^{20–22} In this paper we review a flexible general framework with which to incorporate different prior information simultaneously into the linear inversion.

We explore the use of this framework for simultaneously utilizing spatial and spectral priors. DOT is generally sensitive to four major chromophores in the breast tissue, oxyhemoglobin, deoxyhemoglobin, water, and lipid.²³ Therefore, if we had a spatial prior for some of the chromophores, we would expect an improvement in the reconstruction of all of the chromophores. The MRI method known as the three-point Dixon technique, which separates the MR signal into individual contributions of fat and water in each voxel of tissue, can provide spatial information about water and lipid content in the tissue.²⁴ We propose to obtain the water and lipid spatial distributions from MRI and then to use these as a spatial prior in the DOT image reconstruction of water and lipid while leaving the hemoglobin images unconstrained. Furthermore, this correlation between MRI and DOT

A. Li (angli@nmr.mgh.harvard.edu; Department of Physics) and M. E. Kilmer (Department of Mathematics) are with Tufts University, Medford, Massachusetts 02155. A. Li is also with and Q. Zhang, E. M. C. Hillman, and D. A. Boas are with the Athinoula A. Martinos Center for Biomedical Imaging, Massachusetts General Hospital, Harvard Medical School, Charlestown, Massachusetts 02129. G. Boverman, Y. Zhang, D. Brooks, and E. L. Miller are with the Department of Electrical and Computer Engineering, Northeastern University, Boston, Massachusetts 02115.

Received 20 July 2004; accepted 20 October 2004; revised manuscript received 24 January 2005.

0003-6935/05/101948-09\$15.00/0

© 2005 Optical Society of America

allows us to validate DOT directly with an established imaging modality.

Here we first review a general framework for incorporating different priors into the linear inversion that enables a new approach for DOT in which a spatial prior is directly applied to the reconstruction of physiological parameters. Then we present simulation studies that quantify the improvement in the image contrast-to-noise ratio (CNR) and the reduction of image parameter cross talk afforded by the incorporation of different spatial and spectral priors into the context of imaging breast cancer.

2. Linear Approach to Diffuse Optical Tomography and Its Inverse Solution

A. Linear Approach to Diffuse Optical Tomography

When light enters a highly turbid medium, the individual photons scatter many times and thus trace out random paths before escaping from or being absorbed by the medium. In the highly scattering regime, the optical properties of the turbid medium are described by two parameters: the reduced scattering coefficient $\mu_s'(\mathbf{r}, \lambda)$ and the absorption coefficient $\mu_a(\mathbf{r}, \lambda)$. Photon migration in the highly scattering limit is well approximated by the photon diffusion equation.^{2,25} We further assume that μ_s' is spatially constant. The absorption coefficient μ_a is expressed by two components: the background, $\mu_{a0}(\lambda)$, and the small perturbation between the background and another state, $\delta\mu_a(\mathbf{r}, \lambda)$. The light energy density is expanded in a perturbative series, i.e., $\Phi(\mathbf{r}, \lambda) = \Phi_0(\mathbf{r}, \lambda) + \Phi_1(\mathbf{r}, \lambda) + \dots$, and solved to the first order.^{26,27} The first-order perturbative solution to the heterogeneous equation in the limit in which $\Phi_1 \ll \Phi_0$ is given by

$$\Phi_1(\mathbf{r}_s, \mathbf{r}_d, \lambda) = \int_V -\delta\mu_a(\mathbf{r}, \lambda)\nu D^{-1}G(\mathbf{r}_s, \mathbf{r}, \lambda) \times G(\mathbf{r}, \mathbf{r}_d, \lambda)d^3\mathbf{r}, \quad (1)$$

where \mathbf{r}_s and \mathbf{r}_d are the source and detector locations, respectively; G is the Green's function solution of the diffusion equation for our boundary conditions; ν is the speed of light in the medium; and D is the diffusion coefficient and is equal to $\nu/(3\mu_s')$. We discretize Eq. (1), write it in a matrix-vector form, and further assume additive noise in the measurement:

$$\Phi_1 = \mathbf{A}\mathbf{x} + \mathbf{n}, \quad (2)$$

where \mathbf{n} is measurement noise with a zero-mean random vector; \mathbf{A} is the weight matrix; \mathbf{x} is the vector of the perturbation in the absorption coefficient, $\delta\mu_a$, where each element corresponds to a distinct voxel location; and Φ_1 is a vector of measurements in which each element corresponds to a particular source-detector pair.

B. Inverse Solution

There are various derivations for the linear inverse operator used here. Assuming that both $(\mathbf{A}\mathbf{R}\mathbf{A}^T + \beta\mathbf{C})$ and $(\mathbf{A}^T\mathbf{C}^{-1}\mathbf{A} + \beta\mathbf{R}^{-1})$ are invertible, then the minimization of the expected error, the maximum *a posteriori* estimation when unknowns \mathbf{x} and noise \mathbf{n} are jointly Gaussian distributed (i.e., Bayesian estimation), the Tikhonov regularization, and the generalized Wiener filter all result in the inverse operator (\mathbf{W}):

$$\mathbf{W} = \mathbf{R}\mathbf{A}^T(\mathbf{A}\mathbf{R}\mathbf{A}^T + \beta\mathbf{C})^{-1} \quad (3)$$

and, equivalently,

$$\mathbf{W} = (\mathbf{A}^T\mathbf{C}^{-1}\mathbf{A} + \beta\mathbf{R}^{-1})^{-1}\mathbf{A}^T\mathbf{C}^{-1}, \quad (4)$$

such that the reconstructed image is given by

$$\hat{\mathbf{x}} = \mathbf{W}\Phi^m, \quad (5)$$

where \mathbf{C} is the covariance matrix of \mathbf{n} , \mathbf{R} is the estimated covariance matrix for \mathbf{x} from Eq. (2), β is the regularization parameter, and Φ^m is the measured data corresponding to the prediction Φ_1 . Equation (3) provides a general framework to incorporate different prior information about the covariance of the measurements and the covariance of the tissue optical properties into the inverse solution. A detailed derivation of the inverse operator \mathbf{W} can be found in Dale and Sereno.²⁸ An advantage of the present formulation is that any empirical observations or reasonable assumptions about the second-order statistics of the measurement noise and the perturbations of the optical properties can be explicitly incorporated to constrain the solution.²⁹

Note that Eqs. (3) and (4) are equivalent in principle and that the choice between them can be made on the basis of convenience or computational complexity. In this paper we use Eq. (3).

3. Inverse with Prior Information

In this section we present different formulations for the measurement and solution priors \mathbf{C} and \mathbf{R} , respectively, focusing mainly on the use of spatial and spectral priors in \mathbf{R} .

A. Measurement Prior \mathbf{C}

If we assume that the noise for each measurement is independent of all other measurements and is of equal variance, \mathbf{C} is proportional to the identity matrix. For the simulations in this paper, the standard deviation of the additive noise is varied from measurement channel to measurement channel. In this case the \mathbf{C} matrix is no longer an identity matrix, although it is still diagonal.

Another prior that could be incorporated into \mathbf{C} is systemic physiological signals that interfere with the signals of main interest; examples of such systemic signals include the heartbeat, respiration, and blood

pressure variations. Since these systemic signals are common to multiple-measurement channels and are spatially correlated, they produce a nonzero spatial cross covariance for the data that can be considered in the off-diagonal elements of \mathbf{C} .

B. Spatial Prior in Diagonal Term of \mathbf{R}

Because the inverse imaging problem for DOT is ill posed and generally underdetermined, the image quality is compromised by poor spatial resolution and sensitivity to measurement noise.² This can be improved modestly by optimization of the geometry and the number of measurements,³⁰ but significant improvement can be obtained by inclusion of prior information into the image reconstruction.^{16,19,31,32}

In our previous study of combined three-dimensional (3-D) x-ray mammography and DOT,¹⁸ we utilized an x-ray image as a spatial prior for the DOT reconstruction of a breast lesion. The spatial prior was incorporated as a linear least-squares problem in which the cost function was composed of two terms: the normal data residual term and a second term containing the structural prior. The cost function $f(x)$ is

$$f(\mathbf{x}) = \|\Phi^m - \mathbf{A}\mathbf{x}\|^2 + \beta_1\|(\mathbf{I} - \mathbf{S})\mathbf{x}\|^2 + \beta_2\|\mathbf{S}\mathbf{x}\|^2, \quad (6)$$

where \mathbf{I} is the identity matrix and \mathbf{S} is a diagonal matrix that describes the hypothesized support of the tumor as indicated by the x-ray image. More specifically, in discrete form, the i th element of the diagonal is a 1 if the i th voxel is identified as part of the tumor by the x-ray image and 0 otherwise. β_1 and β_2 are the two regularization parameters that control the degree of regularization in the background and lesion, respectively. The advantage of this method is that the influence of the structural information can be adjusted by appropriately weighting the structural component of the cost function.

This approach of implementing a spatial prior is easily written in the form of Eq. (3). The diagonal of \mathbf{R} varies according to whether the corresponding pixel is inside or outside the region of interest. Specifically, the i th element along the diagonal $\mathbf{R}_{i,i} = \beta_1^{-1}$ when the i th voxel is outside of the region of interest otherwise $\mathbf{R}_{i,i} = \beta_2^{-1}$. A smaller value for β reduces the penalty for the reconstruction of the optical contrast and thus increases the probability of finding contrast in the designated region. Unfortunately, it also increases the image noise in the designated region.³²

C. Spectral Prior

DOT is often used to image the concentration of oxyhemoglobin (HbO_2) and deoxyhemoglobin (HbR) in tissue.^{8,20,33} The technique exploits the fact that oxyhemoglobin and deoxyhemoglobin are the dominant absorbers in the infrared region (650–950 nm). In a typical reconstruction scheme there are three steps to achieve the final HbO_2 and HbR images. First, the measurements are taken simultaneously at two or

more different wavelengths. Second, the images of the absorption coefficients at the different wavelengths are reconstructed separately. Finally, the concentration of HbO_2 and HbR are calculated from the spectral variation in the absorption images. As shown in our previous spectral prior study,²² if images of HbO_2 and HbR are reconstructed directly instead of first reconstructing the spectral absorption images, we can suppress the image noise and reduce the cross talk in the HbO_2 and HbR images by forcing spectral consistency in the reconstructed images.

If we assume that the absorption is dominated by hemoglobin, then

$$\mu_a(\lambda) = \varepsilon_{\text{HbO}_2}(\lambda)[\text{HbO}_2] + \varepsilon_{\text{HbR}}(\lambda)[\text{HbR}], \quad (7)$$

where $\varepsilon_{\text{HbO}_2}$ and ε_{HbR} are the extinction coefficients of HbO_2 and HbR , respectively, which are wavelength dependant; and $[\cdot]$ indicates the concentration of the chromophore. To obtain a unique solution of $[\text{HbO}_2]$ and $[\text{HbR}]$, we need measurements at two different wavelengths at least.

Making use of Eq. (7) allows us to write Φ_1 at two different wavelengths directly in terms of the unknown perturbations to the HbO_2 and HbR concentrations:

$$\begin{bmatrix} \Phi_1(\lambda_1) \\ \Phi_1(\lambda_2) \end{bmatrix} = \begin{bmatrix} \mathbf{A}(\lambda_1) & 0 \\ 0 & \mathbf{A}(\lambda_2) \end{bmatrix} \begin{bmatrix} \delta\mu_a(\lambda_1) \\ \delta\mu_a(\lambda_2) \end{bmatrix} \quad (8a)$$

$$= \mathbf{A}\mathbf{E} \begin{bmatrix} \delta[\text{HbO}_2] \\ \delta[\text{HbR}] \end{bmatrix} \quad (8b)$$

$$= \begin{bmatrix} \varepsilon_{\text{HbO}_2}(\lambda_1)\mathbf{A}(\lambda_1) & \varepsilon_{\text{HbR}}(\lambda_1)\mathbf{A}(\lambda_1) \\ \varepsilon_{\text{HbO}_2}(\lambda_2)\mathbf{A}(\lambda_2) & \varepsilon_{\text{HbR}}(\lambda_2)\mathbf{A}(\lambda_2) \end{bmatrix} \begin{bmatrix} \delta[\text{HbO}_2] \\ \delta[\text{HbR}] \end{bmatrix}, \quad (8c)$$

$$\mathbf{E} = \varepsilon \otimes \mathbf{I}, \quad \mathbf{A} = \begin{bmatrix} \mathbf{A}(\lambda_1) & 0 \\ 0 & \mathbf{A}(\lambda_2) \end{bmatrix},$$

$$\varepsilon = \begin{bmatrix} \varepsilon_{\text{HbO}_2, \lambda_1} & \varepsilon_{\text{HbR}, \lambda_1} \\ \varepsilon_{\text{HbO}_2, \lambda_2} & \varepsilon_{\text{HbR}, \lambda_2} \end{bmatrix}.$$

Notice that \mathbf{E} is the Kronecker product of ε and \mathbf{I} , where the identity matrix \mathbf{I} has dimensions equal to the number of columns of $\mathbf{A}(\lambda_i)$. $\Phi_1(\lambda_1)$ and $\Phi_1(\lambda_2)$ are column vectors of the measurement at wavelengths λ_1 and λ_2 , where each element in the vector represents a different source–detector pair. The measurement arises from spatial variation in the absorption coefficient at each wavelength, as indicated by the vectors $\delta\mu_a(\lambda_1)$ and $\delta\mu_a(\lambda_2)$, where each vector element represents an individual volume element in the highly scattering medium; $\mathbf{A}(\lambda_1)$ and $\mathbf{A}(\lambda_2)$ are the Jacobian matrices of the measurements with respect to changes in the absorption coefficient at each wavelength. The transformation from the spatial variation in the absorption coefficient to the estimated measurement at each wavelength is given by the weight

matrix.² Substitution of Eq. (7) into Eq. (8a) results in Eq. (8c). It is through inversion of the matrix in Eq. (8c) that we are able to reconstruct the images of the physiological parameters [HbO₂] and [HbR] directly, rather than first reconstructing images of the absorption coefficient and then determining the hemoglobin parameters.

Here we show that inversion of Eq. (8b) results in an equation of the form of Eq. (3). We then provide an explanation as to why a spectral prior implemented in this form provides improved image quality. Given a Tikhonov regularization parameter of β , the solution minimizing the cost function between estimated measurements by use of Eq. (8b) and the measurement Φ^m in the least-square sense is

$$\begin{bmatrix} \delta\text{HbO}_2 \\ \delta\text{HbR} \end{bmatrix} = \mathbf{E}^T \mathbf{A}^T (\mathbf{A} \mathbf{E} \mathbf{E}^T \mathbf{A}^T + \beta \mathbf{C})^{-1} \Phi^m. \quad (9)$$

Comparing Eqs. (9) and (3), we see that

$$\mathbf{R} = \mathbf{E} \mathbf{E}^T. \quad (10)$$

Note that \mathbf{R} is no longer a diagonal matrix but a block diagonal matrix. The off-diagonal blocks account for the correlation among the absorption coefficients in the same spatial coordinate at different wavelengths. In effect, solving separately at each wavelength implicitly assumes that the off-diagonal blocks are all zeros. Incorporating the wavelength correlation of the absorption coefficient directly into the inverse solution produces a solution that is optimal, as opposed to the indirect approach that incorrectly assumes that the absorption coefficient is uncorrelated across wavelengths. While incorporating the correlation into the inverse solution is more computationally complex, we demonstrate below that the complexity is justified by the improved image quality.²² This spectral prior is easily extended to consider N unknown chromophores for which the extinction coefficients are known. Of course, measurements at N or more wavelengths are necessary to uniquely determine the chromophore concentrations.

D. Combined Spatial and Spectral Priors

For the sake of simplicity, we consider measurements at two wavelengths. We first write the weight matrix \mathbf{A} in the format $\mathbf{A} = \begin{bmatrix} \mathbf{A}(\lambda_1) & 0 \\ 0 & \mathbf{A}(\lambda_2) \end{bmatrix}$. Given spatial priors for the optical properties at different wavelengths, as in Subsection 3.B, it is straightforward to show that \mathbf{R} should have the form

$$\mathbf{R} = \mathbf{\Omega} \mathbf{E} \mathbf{E}^T \mathbf{\Omega}^T, \quad (11)$$

where $\mathbf{\Omega} = \begin{bmatrix} \sqrt{\mathbf{R}_{\lambda_1}} & 0 \\ 0 & \sqrt{\mathbf{R}_{\lambda_2}} \end{bmatrix}$. Notice that \mathbf{R}_{λ_i} has the same dimension and content as that in Subsection 3.B, except that \mathbf{R}_{λ_i} can vary with wavelength.

Being able to incorporate the spatial and spectral

priors into the reconstruction in one step is useful. Since each prior alone has been shown to improve the image quality, we would expect to further optimize the reconstruction by combining two priors. The simplicity of combining these different priors shows the flexibility of the form of Eq. (3). This format will be quite useful if we have reasonable assumptions, or priors provided by some other image modality, about the optical properties of the tissue.

If we want to incorporate spatial priors directly onto the chromophores instead of onto the optical properties, \mathbf{R} should have the following structure:

$$\mathbf{R} = \mathbf{E} \mathbf{\Omega} \mathbf{\Omega}^T \mathbf{E}^T \quad (12)$$

where

$$\mathbf{\Omega} = \begin{bmatrix} \sqrt{\mathbf{R}_{\text{HbO}_2}} & 0 \\ 0 & \sqrt{\mathbf{R}_{\text{HbR}}} \end{bmatrix}$$

Now $\mathbf{R}_{\text{HbO}_2}$ and \mathbf{R}_{HbR} are the *a priori* covariance matrices for the chromophores. This format is useful if we have reasonable assumptions, or priors provided by other image modality, about the spatial variations in concentration of the chromophores of the tissue. We detail an example of this in Subsection 3.E.

E. Example of Direct Imaging of Absorbing Chromophores with Magnetic Resonance Imaging Providing Water and Lipid Spatial Priors

For diffuse optical imaging of breast cancer, the dominant absorbing chromophores in the near infrared are oxyhemoglobin, deoxyhemoglobin, water, and lipid, with the spectral variation in the absorption coefficient given by

$$\mu_a(\lambda) = \varepsilon_{\text{HbO}_2}(\lambda)[\text{HbO}_2] + \varepsilon_{\text{HbR}}(\lambda)[\text{HbR}] + \varepsilon_{\text{H}_2\text{O}}(\lambda)[\text{H}_2\text{O}] + \varepsilon_{\text{lipid}}(\lambda)[\text{Lipid}]. \quad (13)$$

MRI has been shown to quantify water and lipid content in tissue. Water and lipid content can be determined with the three-point Dixon technique.²⁴ We can utilize these MR images as spatial priors for the water and lipid optical images. The MRI priors can be imposed as either a soft or hard constraint in the water and lipid image reconstruction. To impose this spatial prior on the chromophores, the \mathbf{R} in Eq. (3) should use the expression in Eq. (12), where

$$\mathbf{\Omega} = \begin{bmatrix} \sqrt{\mathbf{R}_{\text{HbO}_2}} & 0 & 0 & 0 \\ 0 & \sqrt{\mathbf{R}_{\text{HbR}}} & 0 & 0 \\ 0 & 0 & \sqrt{\mathbf{R}_{\text{H}_2\text{O}}} & 0 \\ 0 & 0 & 0 & \sqrt{\mathbf{R}_{\text{lipid}}} \end{bmatrix}. \quad (14)$$

$\mathbf{R}_{\text{HbO}_2}$, \mathbf{R}_{HbR} , $\mathbf{R}_{\text{H}_2\text{O}}$, and $\mathbf{R}_{\text{lipid}}$ are all diagonal matrices. Our working hypothesis is that there is a positive correlation between local water and lipid chromophores of DOT and local water and lipid MRI con-

Table 1. Chromophore Content of the Background Medium and the Absorbing Objects

Inclusions	HbO ₂ (μM)	HbR (μM)	Water (%)	Lipid (%)
Background	25	10	40	30
δHbO_2 (object 1)	45	10	40	30
δHbR (object 2)	25	20	40	30
δWater (object 3)	25	10	70	30
δLipid (object 4)	25	10	40	50

trast. The diagonal elements of each of the four matrices encode the prior estimates of the spatial variance in the corresponding chromophore concentrations. We can therefore incorporate the MRI prior on water and lipid content in $\mathbf{R}_{\text{H}_2\text{O}}$ and $\mathbf{R}_{\text{lipid}}$ as a monotonically increasing function of the corresponding MRI contrast. In this example we assume that we do not have prior spatial information for $\mathbf{R}_{\text{HbO}_2}$ or \mathbf{R}_{HbR} , and thus $\mathbf{R}_{\text{HbO}_2}$ and \mathbf{R}_{HbR} are identity matrices. Previous research has shown that incorporation of physiological priors of hemoglobin and spatial priors improves the image quality.¹⁹ Another more straightforward way to use the spatial MRI water and lipid prior is to simply take the MRI water and lipid content estimate as the DOT water and lipid content. The validity of such a strict correspondence requires *in vivo* verification. Although Merritt *et al.* have shown a 100% correlation in phantoms,³⁴ for now we consider the statistical correlation. In Subsection 4.B we describe a simulation to demonstrate the improvement in DOT image quality provided by an MRI spatial prior for water and lipid. We note that the incorporation of multiple priors as described in Subsection 3.D is necessary to utilize a spatial prior on a specific chromophore. Utilizing the same spatial prior on the absorption coefficient instead of on the specific chromophore would likely degrade the image quality.

4. Simulation Results

We performed simulations in the context of imaging breast cancer to demonstrate the improvement in image quality that arises from spectral priors, as in Eq. (10), and the further improvement with both spectral priors and spatial priors on water and lipid content as provided by MRI, as in Eq. (12).

For the simulations, we considered four chromophores: HbO₂, HbR, water, and lipid. Four spherical absorbing objects were embedded in an otherwise homogeneous slab-geometry medium. The diameter of each object was 2 cm, and the thickness of the slab was 6 cm. The composition of the background was chosen to be similar to that of a young woman's breast.²³ The chromophore content of the background medium and of each object is listed in Table 1. The positions of the four objects are shown in Fig. 1. The spectral variation of the scattering coefficient is assumed to have the form $\mu_s' = a\lambda^{-\text{SP}}$, where a is a constant, λ is the wavelength in nanometers, and SP is the scatter power. In all of the simulations, we

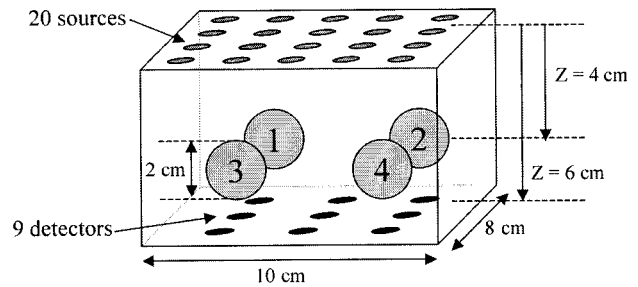


Fig. 1. Four targets are embedded in the homogeneous background in the simulations. All targets have a diameter of 2 cm. Targets 1, 2, 3, and 4 are HbO₂, HbR, water, and lipid perturbations, respectively.

assume that μ_s' is spatially uniform throughout the medium; a and SP are given the values 2200 and 0.83, respectively.²³

Simulated measurements are generated with the analytical Born approximation in slab geometry at six wavelengths: 685, 750, 808, 830, 930, and 960 nm. These wavelengths were chosen to keep the condition number of the extinction matrix ϵ small. According to Corlu *et al.*,²¹ wavelengths that minimize this condition number will reduce the cross talk among the chromophores. The positions of sources and detectors are shown in Fig. 1.

The sources are rf modulated at 70 MHz. There are 20 sources and 9 detectors placed in a transmission geometry, as indicated in Fig. 1. Both shot noise and electronic noise are included in the data, and the noise is uncorrelated from channel to channel. The noise model is based on our frequency-domain instrument and is fully described in Ref. 35. We control the parameters so that the noise is shot-noise limited at high signal-to-noise ratios (SNRs) and the electronic noise limited at low SNRs. The range of the SNR across measurements at each wavelength is listed in Table 2. For the reconstructions, we assume that we know the measurement standard deviation and use this information in the covariance matrix \mathbf{C} of the linear inverse operator Eq. (3).

A. Improvements with a Spectral Prior

An example comparison of the reconstructed HbO₂, HbR, H₂O, and lipid images without and with spectral priors is shown in Figs. 2 and 3, respectively. More specifically, Fig. 2 is generated by reconstruction of μ_a images at six wavelengths, followed by a pixel-by-pixel calculation of the concentration of each chromophore. Figure 3 is generated by calculation of

Table 2. Range of SNR Measurements at Each Wavelength

SNR Measurement	Source Wavelength (nm)					
	685	750	808	830	930	960
Maximum SNR (dB)	67	69	71	69	51	37
Percentage of channels with SNR above 20 dB	90%	91%	97%	99%	82%	37%

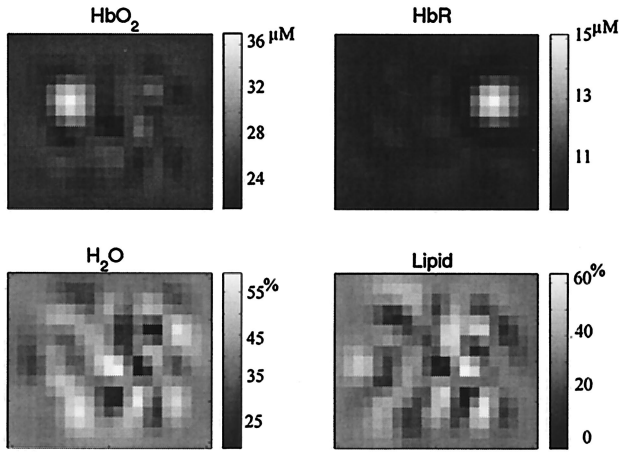


Fig. 2. Physiological image reconstruction without any prior information, using simulated data. The images are shown for the slice at a depth of 4 cm where the true objects are centered. β_r is set to 0.0005. The field of view of the image is 8 cm \times 10 cm.

the chromophore concentrations directly with spectral priors, as in Eq. (9). The images are shown for the slice at a depth of 4 cm where the true objects are centered. In the reconstruction we assume that the background tissue properties are known. After obtaining the perturbation images, we added the background properties. The regularization parameter β has different effects on the resolution of the two different imaging procedures. We therefore altered the regularization parameter for each to equalize the FWHM of the reconstructed HbO₂ object. If we define $\beta = \beta_r \cdot \max(\mathbf{A}\mathbf{R}\mathbf{A}^T)$, for the cases in Figs. 2 and 3, β_r is equal to 0.0005 without spectral priors (i.e., $\mathbf{R} = \mathbf{I}$) and 0.0001 with spectral priors. The improvement in the reconstruction with priors is obvious in terms of the CNR of the image. The H₂O and lipid reconstructions without spectral priors are too noisy

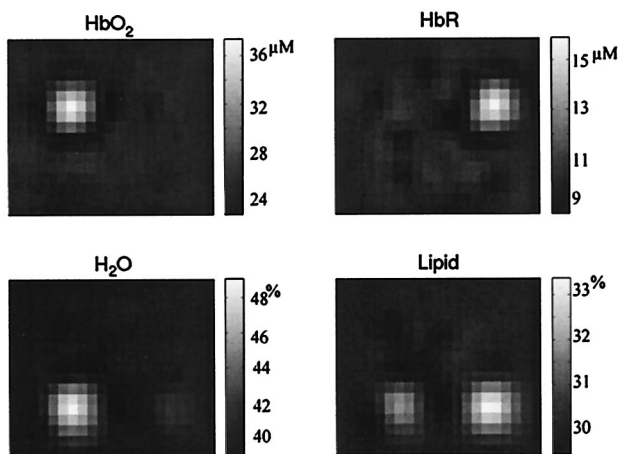


Fig. 3. Physiological image reconstruction with a spectral prior, using simulated data. The images are shown for the slice at a depth of 4 cm where the true objects are centered. β_r is set to 0.0001. The FWHM of the reconstructed HbO₂ object is the same as the one in the reconstruction without a prior, which is shown in Fig. 2. The field of view of the image is 8 cm \times 10 cm.

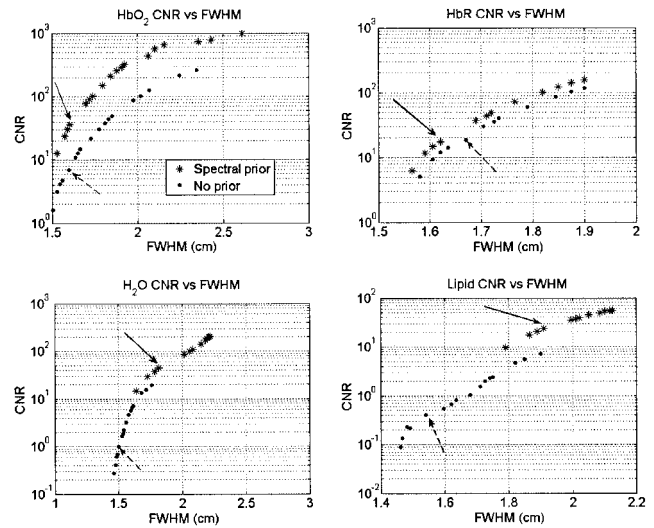


Fig. 4. Plot of the CNR versus the FWHM of the reconstructed images without and with spectral priors, using simulated data. Dashed arrow, CNR and FWHM in the reconstruction shown in Fig. 2; solid arrow, values in the reconstruction shown in Fig. 3.

to see any heterogeneity. Note that the H₂O and lipid CNRs can be improved by increasing the regularization at the expense of resolution, as discussed in more detail by the end of this paragraph. The issue of cross talk among different chromophores is more complicated and is discussed in more detail the next paragraph. To compare the reconstructions quantitatively, we calculated the CNR, FWHM, and cross talk among the different chromophores, given a set of regularization parameters ($10^{-5} \leq \beta_r \leq 10$). The CNR is given by the peak value of the reconstructed contrast divided by the mean standard deviation of every voxel in the image. The mean standard deviation is the statistical result of 100 independent noise simulations for each regularization parameter. In Fig. 4, we plot the log (CNR) versus the FWHM. Generally, over a wide range of regularization parameters β , the reconstruction of all four chromophores with a spectral prior has a better CNR than that without a spectral prior. One can argue that the better CNR in the water and lipid images results from a loss of spatial resolution; however, the dramatic improvement in CNR is worth the small loss in resolution. To facilitate the comparison of the images in Figs. 2 and 3 with the results in Fig. 4, the dashed and solid arrows in Fig. 4 indicate the CNR and FWHM of the reconstructions in Figs. 2 and 3, respectively.

The CNR improvement obtained with the spectral priors is expected since the reconstruction with the priors exploits the fact that optical properties within a voxel are correlated across wavelengths. The comparison of the cross talk between chromophores does not yield a clear message. Here we define cross talk of chromophore i into j as the measured contrast j divided by the measured contrast in i at a location where the true object has contrast only in chromophore i . From our simulations, we found that in

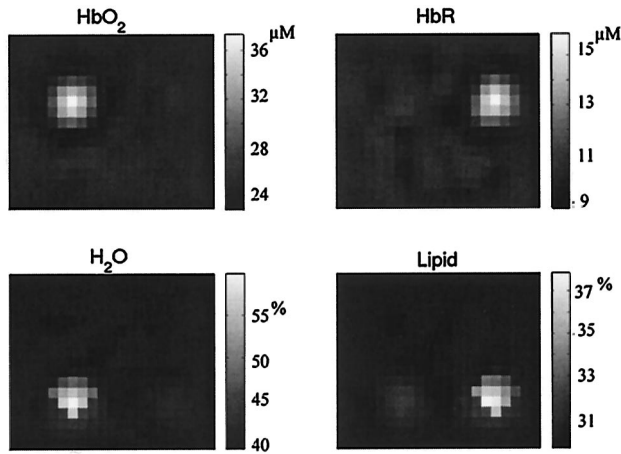


Fig. 5. Physiological image reconstruction with both spectral and spatial priors for water and lipid content, using simulated data. The images are shown for the slice at a depth of 4 cm where the true objects are centered. β_r is set to 0.0001. The FWHM of the reconstructed HbO_2 object is same as that in the reconstruction without a prior, which is shown in Fig. 2. The field of view of the image is $8 \text{ cm} \times 10 \text{ cm}$.

most cases, use of a spectral prior yields a cross-talk reduction (results not shown). However, some increase in the cross talk between, for example, HbO_2 and HbR was observed upon incorporation of the spectral prior, although particular choices of wavelength combinations have been shown to have a strong effect on cross talk.²¹ Since we consider only a single set of wavelengths here, conclusions about the efficacy of using spectral priors based on cross talk would be misleading. We intend to continue investigating optimal wavelength combinations further to identify combinations that yield substantial improvements in image CNR and image cross talk.

B. Case Comparison of Reconstruction with Spectral Prior and with both Spectral and Magnetic Resonance Image Spatial Priors

The method of adding MRI water and lipid spatial priors to the reconstruction is described as follows. We assume that the MRI water and lipid contrast and optical contrast are well correlated. We further assume that MR images yield an accurate estimation of the water and lipid content. We take the simulated equivalent of normalized MR images and add them in the diagonal $\mathbf{R}_{\text{H}_2\text{O}}$ and $\mathbf{R}_{\text{lipid}}$ term of $\mathbf{\Omega}$ in Eq. (14). This soft constraint technique provides the reconstruction prior information about the location and amplitude of the water and lipid perturbations, but it does not constrain the optical image to explicitly match the MRI prior. Figure 5 shows the reconstruction with both spectral priors and water and lipid spatial priors, using Eq. (12). Figure 6(b) shows all the water and lipid Z slices of the 3-D reconstruction shown in Fig. 5 to demonstrate the improved Z resolution achieved when both spectral and spatial priors are used. Figure 6(a) illustrates the Z resolution achieved when only spectral priors are included in the reconstruction. The regularization parameter that we

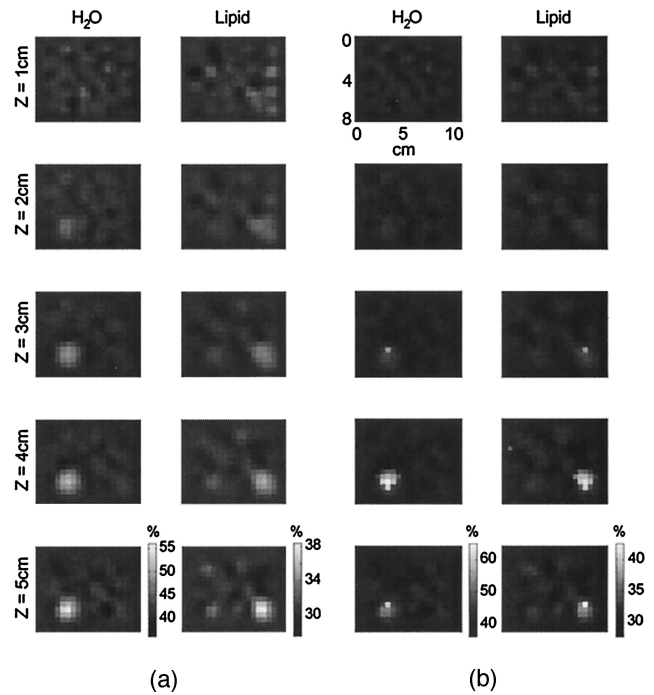


Fig. 6. (a) The 3-D display of water and lipid image reconstruction with the spectral prior, using simulated data. (b) The 3-D display of water and lipid image reconstruction with both spectral and spatial priors, using simulated data.

choose is the same as the one in the reconstruction with only spectral priors (shown in Fig. 3). Comparing Figs. 3 and 6(a), we see that the improvement in CNR and spatial resolution for the water and lipid images is significant in both the lateral (Fig. 5) and the axial [Fig. 6(b)] directions. The HbO_2 and HbR images are comparable with those obtained with only the spectral priors (Fig. 3), since no spatial information was provided for the hemoglobin.

Note that we could also use the water and lipid content derived from MR images as a fixed prior for optical imaging. By assuming that these parameters are already known, our optical imaging problem would be simplified to only a two-parameter reconstruction (HbO_2 and HbR), while including the effects of the known water and lipid content into the optical solution. We would expect this approach to improve the optical image quality for HbO_2 and HbR , as suggested by Schweiger and Arridge.³¹

5. Summary

We have described and illustrated a flexible framework for including single and multiple priors in the linear DOT image reconstruction. This framework enables us to impose spatial priors directly on the physiological parameters of interest rather than on the optical properties derived from multiple physiological processes. We illustrated the improvements to image CNR achieved when spectral priors are incorporated into the direct reconstruction of HbO_2 , HbR , H_2O , and lipid. We also demonstrated the advantage of also imposing spatial priors on the physiological

parameters, such as those accessible via MR images of water and lipid content.

It is a pleasure to acknowledge the fruitful discussions with Solomon Diamond and Theodore Huppert. This study was supported in part by Advanced Research Technologies; by National Institutes of Health grants R01-CA97305 and U54-CA105480; and by CenSSIS, the Center for Subsurface Sensing and Imaging Systems, under the Engineering Research Center's Program of the National Science Foundation (award EEC-9986821).

References

1. A. Yodh and B. Chance, "Spectroscopy and imaging with diffusing light," *Phys. Today* **48**, 34–40 (1995).
2. S. R. Arridge, "Optical tomography in medical imaging," *Inverse Probl.* **15**, R41–R93 (1999).
3. D. A. Boas, D. H. Brooks, E. L. Miller, C. A. DiMarzio, M. Kilmer, R. J. Gaudette, and Q. Zhang, "Imaging the body with diffuse optical tomography," *IEEE Signal Process. Mag.* **18**, 57–75 (2001).
4. E. Okada, M. Firbank, M. Schweiger, S. R. Arridge, M. Cope, and D. T. Delpy, "Theoretical and experimental investigation of near-infrared light propagation in a model of the adult head," *Appl. Opt.* **36**, 21–31 (1997).
5. B. Chance, E. Anday, S. Nioka, S. Zhou, L. Hong, K. Worden, L. C. T. Murray, Y. Ovetsky, D. Pidikiti, and R. Thomas, "A novel method for fast imaging of brain function, non-invasively, with light," *Opt. Express* **2**, 411–423 (1998), <http://www.opticsexpress.org>.
6. A. Bluestone, G. Abdoulaev, C. Schmitz, R. Barbour, and A. Hielscher, "Three-dimensional optical tomography of hemodynamics in the human head," *Opt. Express* **9**, 272–286 (2001), <http://www.opticsexpress.org>.
7. M. A. Franceschini and D. A. Boas, "Noninvasive measurement of neuronal activity with near-infrared optical imaging," *Neuroimage* **21**, 372–386 (2004).
8. B. W. Pogue, S. P. Poplack, T. O. McBride, W. A. Wells, K. S. Osterman, U. L. Osterberg, and K. D. Paulsen, "Quantitative hemoglobin tomography with diffuse near-infrared spectroscopy: pilot results in the breast," *Radiology* **218**, 261–266 (2001).
9. J. C. Hebden, H. Veenstra, H. Dehghani, E. M. C. Hillman, M. Schweiger, S. R. Arridge, and D. T. Delpy, "Three-dimensional time-resolved optical tomography of a conical breast phantom," *Appl. Opt.* **40**, 3278–3287 (2001).
10. H. Jiang, Y. Xu, N. Iftimia, J. Eggert, K. Klove, L. Baron, and L. Fajardo, "Three-dimensional optical tomographic imaging of breast in a human subject," *IEEE Trans. Med. Imaging* **20**, 1334–1340 (2001).
11. R. Barbour, H. Graber, Y. Pei, S. Zhong, and C. Schmitz, "Optical tomographic imaging of dynamic features of dense-scattering media," *J. Opt. Soc. Am. A* **18**, 3018–3036 (2001).
12. E. M. C. Hillman, J. C. Hebden, M. Schweiger, H. Dehghani, F. E. W. Schmidt, D. T. Delpy, and S. R. Arridge, "Time resolved optical tomography of the human forearm," *Phys. Med. Biol.* **46**, 1117–1130 (2001).
13. Y. Xu, N. Iftimia, H. B. Jiang, L. L. Key, and M. B. Bolster, "Imaging of *in vitro* and *in vivo* bones and joints with continuous-wave diffuse optical tomography," *Opt. Express* **8**, 447–451 (2001), <http://www.opticsexpress.org>.
14. A. Hielscher, A. Bluestone, G. Abdoulaev, A. Klose, J. Lasker, M. Stewart, U. Netz, and J. Beuthan, "Near-infrared diffuse optical tomography," *Dis. Markers* **18**, 313–337 (2002).
15. V. Ntziachristos, A. G. Yodh, M. Schnall, and B. Chance, "Concurrent MRI and diffuse optical tomography of breast after Indocyanine Green enhancement," *Proc. Natl. Acad. Sci. USA* **97**, 2767–2772 (2000).
16. B. A. Brooksby, H. Dehghani, B. W. Pogue, and K. D. Paulsen, "Near-infrared (NIR) tomography breast image reconstruction with *a priori* structural information from MRI: algorithm development for reconstructing heterogeneities," *IEEE J. Sel. Top. Quantum Electron.* **9**, 199–209 (2003).
17. Q. Zhu, T. Durduran, V. Ntziachristos, M. Holboke, and A. G. Yodh, "Imager that combines near-infrared diffusive light and ultrasound," *Opt. Lett.* **24**, 1050–1052 (1999).
18. A. Li, E. L. Miller, M. E. Kilmer, T. J. Brukilacchio, T. Chaves, J. Stott, Q. Zhang, T. Wu, M. Chorlton, R. H. Moore, D. B. Kopans, and D. A. Boas, "Tomographic optical breast imaging guided by three-dimensional mammography," *Appl. Opt.* **42**, 5181–5190 (2003).
19. X. Intes, C. Maloux, M. Guven, B. Yazici, and B. Chance, "Diffuse optical tomography with physiological and spatial *a priori* constraints," *Phys. Med. Biol.* **49**, N155–N163 (2004).
20. E. M. C. Hillman, "Experimental and theoretical investigations of near infrared tomographic imaging methods and clinical applications," Ph.D. dissertation (University of London, London, UK, 2002).
21. A. Corlu, T. Durduran, R. Choe, M. Schweiger, E. M. C. Hillman, S. R. Arridge, and A. G. Yodh, "Uniqueness and wavelength optimization in continuous-wave multispectral diffuse optical tomography," *Opt. Lett.* **28**, 2339–2341 (2004).
22. A. Li, Q. Zhang, J. P. Culver, E. L. Miller, and D. A. Boas, "Reconstructing chromosphere concentration images directly by continuous-wave diffuse optical tomography," *Opt. Lett.* **29**, 256–258 (2004).
23. A. E. Cerussi, A. J. Berger, F. Bevilacqua, N. Shah, D. Jakubowski, J. Butler, R. F. Holcombe, and B. J. Tromberg, "Sources of absorption and scattering contrast for near-infrared optical mammography," *Acad. Radiol.* **8**, 211–218 (2001).
24. G. Glover and E. Schneider, "3-point Dixon technique for true water fat decomposition with BO inhomogeneity correction," *Magn. Reson. Med.* **18**, 373–381 (1991).
25. M. A. O'Leary, "Imaging with diffuse photon density waves," Ph.D. dissertation (University of Pennsylvania, Philadelphia, Pa., 1996).
26. M. S. Patterson, B. Chance, and B. C. Wilson, "Time resolved reflectance and transmittance for the noninvasive measurement of tissue optical properties," *Appl. Opt.* **28**, 2331–2336 (1989).
27. B. W. Pogue and M. S. Patterson, "Frequency-domain optical-absorption spectroscopy of finite tissue volumes using diffusion-theory," *Phys. Med. Biol.* **39**, 1157–1180 (1994).
28. A. Dale and M. Sereno, "Improved localization of cortical activity by combining EEG and MEG with MRI cortical surface reconstruction—a linear approach," *J. Cogn. Neurosci.* **5**, 162–176 (1993).
29. A. Liu, A. Dale, and J. Belliveau, "Monte Carlo simulation studies of EEG and MEG localization accuracy," *Hum. Brain Mapp.* **16**, 47–62 (2002).
30. J. P. Culver, V. Ntziachristos, M. J. Holboke, and A. G. Yodh, "Optimization of optode arrangements for diffuse optical tomography: a singular-value analysis," *Opt. Lett.* **26**, 701–703 (2001).
31. M. Schweiger and S. R. Arridge, "Optical tomographic reconstruction in a complex head model using *a priori* region boundary information," *Phys. Med. Biol.* **44**, 2703–2721 (1999).
32. B. W. Pogue, T. O. McBride, J. Prewitt, U. L. Osterberg, and K. D. Paulsen, "Spatially variant regularization improves diffuse optical tomography," *Appl. Opt.* **38**, 2950–2961 (1999).

33. D. J. Hawrysz and E. M. Sevick-Muraca, "Developments toward diagnostic breast cancer imaging using near-infrared optical measurements and fluorescent contrast agents," *Neoplasia* **2**, 388–417 (2000).
34. S. Merritt, G. Gulsen, G. Chiou, Y. Chu, C. Deng, A. Cerussi, A. Durkin, B. Tromberg, and O. Nalcioglu, "Comparison of water and lipid content measurements using diffuse optical spectroscopy and MRI in emulsion phantoms," *Technol. Cancer Res. Treat.* **2**, 563–569 (2003).
35. R. J. Gaudette, D. H. Brooks, C. A. DiMarzio, M. E. Kilmer, E. L. Miller, T. Gaudette, and D. A. Boas, "A comparison study of linear reconstruction techniques for diffuse optical tomographic imaging of absorption coefficient," *Phys. Med. Biol.* **45**, 1051–1070 (2000).